RESEARCH ARTICLE

Synthesis and Characterization of Tin Oxide Quantum Dots: Effect of pH and Temperature on Structural and Optical Properties

Maryam Amoo[1], Atefe Marasi[2]*

[1] Department of Materials Engineering, Isfahan University of Technology, Isfahan 84156-83111, Iran
[2] Department of Physics, Faculty of Science, University of Isfahan, HezarJerib, 81746-73441, Isfahan, Iran

ARTICLE INFO

Article History:

Received 2025-09-15
Accepted 2025-12-31
Published 2024-05-05

Keywords:

Tin monoxide (SnO),
Quantum Dots,
Co-precipitation,
Optical Properties,
Nanomaterials.

ABSTRACT

In this study, we report the synthesis of Tin Oxide Quantum Dots using a co-precipitation method, with an emphasis on SnO, the lesser-studied monoxide phase of tin. While extensive research has been conducted on SnO_2 due to its superior chemical stability and wide-ranging applications in gas sensing and catalysis, limited attention has been paid to SnO, which presents unique optical and electronic properties. Here, SnO quantum dots were synthesized under controlled pH and drying conditions. X-ray diffraction confirmed the formation of tetragonal SnO with an average crystallite size of ~13 nm. UV-Vis absorption spectra revealed distinct peaks at ~400 nm, 290 nm and 240 nm, with systematic red/blue shifts observed under varying pH and thermal conditions. Photoluminescence emission spectra showed characteristic peak growth correlated with absorption edge excitations. Scanning tunneling microscopy confirmed particle sizes around 20 nm. The results suggest that SnO QDs have significant potential for use in optoelectronic devices, Li-ion batteries and gas sensors.

How to cite this article
Amoo M., Marasi A., Synthesis and Characterization of Tin Oxide Quantum Dots: Effect of pH and Temperature on Structural and Optical Properties. J. Nanoanalysis., 2024; 11(2): 729-741.

INTRODUCTION

Since the discovery of size-dependent properties in nanomaterials, quantum dots (QDs) have gained remarkable attention due to their unique optical, electronic, and catalytic characteristics. Among various types of QDs, metal oxide-based quantum dots have shown considerable potential, especially in fields such as optoelectronics, catalysis, and energy storage devices. Tin-based oxides, particularly tin(IV) oxide (SnO_2) and tin(II) oxide (SnO), are of special interest

*Corresponding Author Email: *maryam.amoo@ma.iut.ac.ir*

due to their semiconducting nature and wide range of applications [1].

SnO_2, a well-known n-type wide-bandgap semiconductor, has been extensively studied and widely applied in gas sensors [2], solar cells [3, 4], photocatalysts [5], supercapacitors [6] and lithium-ion batteries [2] due to its stability and availability. In contrast, tin (II) oxide (SnO), a p-type narrow-bandgap semiconductor, has remained relatively underexplored, mainly due to its lower stability and synthesis challenges. However, recent studies suggest that SnO exhibits promising photoelectronic properties such as higher carrier mobility and favorable band alignment, which could surpass those of SnO_2 in certain applications [7, 8].

Several synthesis methods have been employed for fabricating SnO nanostructures, including hydrothermal [9], sonochemical [10], combustion, sol-gel [11] and co-precipitation techniques. Among these, the co-precipitation method offers a simple, low-cost, and scalable approach for producing quantum dots with controlled size and morphology [12].

The aim of this research is to synthesize SnO quantum dots using the co-precipitation method and to investigate their structural and optical properties. Furthermore, the effects of various synthesis parameters such as pH, temperature, and drying atmosphere on the phase formation and quantum confinement behavior of SnO QDs are systematically studied.

EXPERIMENTAL

Sample synthesis

SnO Quantum dots were synthesized via a controlled co-precipitation technique. A 0.005 M aqueous solution of Tin (II) chloride dihydrate Merck, $SnCl_2 \cdot 2H_2O$ (99%, 107815) was prepared in 150 mL of deionized water. Subsequently, 7 mL of concentrated HCl (37%, Merck, 100317) was added dropwise under constant stirring until the pH reached 1. Then Ammonium hydroxide (25%, Merck, 1336-21-6) was dropped to adjust the pH to target values between 8 and 10. The resulting precipitate was centrifuged at 3500 rpm for 10 minutes, thoroughly washed with deionized water and ethanol and then dried under varied thermal and atmospheric conditions (e.g., vacuum, air, and furnace drying). A total of 20 samples (coded s1–b4) were synthesized with varying synthesis temperatures, pH levels and drying environments. **Table 1** summarizes the synthesis parameters.

Instrumental analysis

To characterize the structural and optical properties of the synthesized samples, several instrumental techniques were employed:

X-ray Diffraction (XRD):

The sample characterization was done using X-ray diffraction (XRD- X'Pert Pro MPD-PANalytical) diffractometer with Cu Kα radiation (λ = 1.5406 Å) over a 2θ range of 15° to 80°. β is the Full Width at Half Maximum (FWHM) and θ is the Bragg's diffraction angle[7]. The average crystallite size (D) was calculated using the Scherrer equation (1): [13]

$$D=0.9\lambda\beta\cos\theta \quad (1)$$

Data were analysed by Expert App. Lattice constants were calculated using Equation (2), suitable for tetragonal crystal systems:

$$a^{-2}+b^{-2}+c^{-2}=d^2 \quad (2)$$

Scanning Tunneling Microscopy (STM):

STM (SS3-Pars Nano system), was used to study surface morphology and estimate the particle size distribution of the synthesized samples.

UV–Visible Spectroscopy (UV–Vis):

Absorption spectra were recorded using a T70 UV–Vis Spectrometer and photoluminescence spectroscopy (PL) (PG Instruments Ltd). The band gap energy (Eg) was calculated from the absorption edge using the following relation (3):

$Eg=h(c/\lambda) = h\nu$ (3)

Using Planck's constant $h=4.13567\times10^{-15}$ eV.s and the speed of light $c=2.99792458\times10^{8}$ m.s^{-1}, Equation simplifies is (4):

$Eg(eV)=1240\ (eV.nm) /\lambda_{max}(nm)$ (4)

As the absorption edge shifts to shorter wavelengths (blue shift), the band gap increases. This is attributed to quantum confinement effects, analogous to a particle-in-a-box model, where smaller particles exhibit discrete energy levels [14].

Particle Size from Band Gap:

The particle radius (R) was estimated from the calculated band gap energy using Equation (5), derived from the effective mass approximation:

$\Delta Eg= Eg^{nano} - Eg^{bulk} = \hbar^2\pi^2 / 2MR^2$ (5)

Here, Eg^{nano} and Eg^{bulk} are the band gaps of the nanoparticle and bulk material respectively, ħ is the reduced Plank constant, R is the radius of nanoparticles and M is the reduced mass of exciton defined by:

$1/M = 1/m_e^* + 1/m_h^*$ (6)

where m_e^* and m_h^* are the effective masses of electrons and holes, respectively [7].

Table1: sample codes and synthesis conditions

Sample cods	Synthesizes temperature	pH	Drying temperature	Drying atmosphere
s1	30	8	30	Oven
s2	30	8.5	30	Oven
s3	30	9	30	Oven
s4	30	9.5	30	Oven
s5	30	10.5	30	Oven
t1	30	8	150	Oven
a1	30	8	50	Vacuum
a2	30	8	90	Vacuum
a3	30	8	150	Vacuum
a4	30	9	50	Vacuum
a5	30	9	90	Vacuum
a6	30	9	150	Vacuum
a7	30	10	50	Vacuum
a8	30	10	90	Vacuum
a9	30	10	150	Vacuum
b1	7	8	30	Air
b2	30	8	30	Air
b3	65	8	30	Air
b4	85	8	30	Air

Tauc Plot and Band Gap Nature:

The type of electronic transition and band gap value was determined using the Tauc relation (7): [15]

$(\alpha h\nu)^n = B(h\nu - E_g)$ (7)

The parameter n in Equation (6) is determined by the nature of the electronic transition and may take values of 0.5, 2, 1.5, or 3, which correspond to, allowed direct, and allowed indirect, forbidden direct and forbidden indirect transitions, respectively. The constant B is a material-dependent factor associated with the transition type and the directness of the optical band gap [15, 16].

Urbach Energy (Eu):

Urbach energy, which quantifies the degree of structural disorder and tail states in the band gap, was calculated using the exponential Urbach relation (8): [15]

$\alpha = \alpha_0 \exp[E/E_u]$ (8)

Here, α0 is a constant, E is photon energy and Eu is the Urbach energy (The energy difference between the excitonic absorption edge and the conduction band edge). Therefore, the Urbach energy can be determined from the inverse of the slope of the linear region of the plot of ln(α) versus photon energy (hν) [17].

Activation Energy (Ea):

Activation energy (Ea) represents the minimum energy barrier that must be overcome for a chemical reaction to proceed, often associated with bond dissociation and molecular rearrangement. According to the Arrhenius equation, a decrease in Ea leads to an increased reaction rate, as temperature contributes to overcoming this energy barrier regardless of whether the reaction is endothermic or exothermic. In this study, Ea was determined using the Arrhenius-type relation for samples synthesized at various temperatures, reflecting the particle growth kinetics. Lower Ea values correspond to faster nucleation and growth processes, indicative of fewer energetic constraints during synthesis [17]:

$E = -RT \ln (d/a)$ (9)

- E is activation energy,
- T is the synthesis temperature in Kelvin,
- d is the average crystallite size,
- a is the intercept,
- R= (8.314 J/K.mol) is the gas constant.

RESULTS AND DISCUSSIONS

Characteristics of nanocatalysts

XRD Analysis:

Figure 1(A) shows the XRD pattern of sample s1, matched with JCPDS cards 01-084-2157 ($Sn_6O_4(OH)_4$) and 00-006-0395 (SnO) [10]. The presence of the intermediate phase $Sn_6O_4(OH)_4$ indicates partial conversion. Additional peak near $2\theta \approx 33°$ corresponds to SnO. The peaks are slightly shifted compared to the reference, suggesting lattice contraction, typical of nanoscale materials. The average crystallite size was calculated as **34 nm** using Equation (1). Lattice parameters obtained from Equation (2) were: (a = b = 7.924 Å, c = 9.100 Å). These are slightly smaller than reference values (a = b = 7.9268 Å, c = 10.25 Å), confirming lattice shrinkage due to size reduction [18].

Figure 1(B) corresponds to sample a1, primarily SnO with minor SnO_2 impurities, matched with JCPDS 01-085-0423 and 00-003-0439, respectively. The lattice constants for SnO were: (a = b = 3.6857 Å, c = 3.3133 Å)

Compared to reference values (a = b = 3.7986 Å, c = 4.8408 Å), the diffraction peaks shifted to higher angles, suggesting lattice expansion. Crystallite sizes were calculated as: (SnO: ~13 nm, SnO_2: ~7 nm)

Figure 1(C) illustrates the XRD pattern of sample **t1**, indicating complete transformation to pure SnO_2 phase after annealing at 100 °C. The pattern perfectly matches JCPDS card 00-001-0657, confirming the formation of single-phase tetragonal SnO_2. The calculated lattice constants were: (a = b =

4.742 Å, c = 3.190 Å). Average crystallite size was found to be ~4 nm, suggesting quantum-sized SnO_2 particles [19].

STM Morphology:

Figure 2 displays the STM image of sample **a1**. The average particle size was found to be approximately **20 nm**, consistent with XRD findings and indicating relatively uniform size distribution [7].

Optical Characterization and Band Gap Analysis

Effect of Temperature at pH 8:

(Figure 3) A blue shift of the ~228 nm peak indicates size reduction; disappearance of the ~296 nm shoulder suggests SnO_2 formation; shifting of the ~369 nm peak implies broader size distribution.

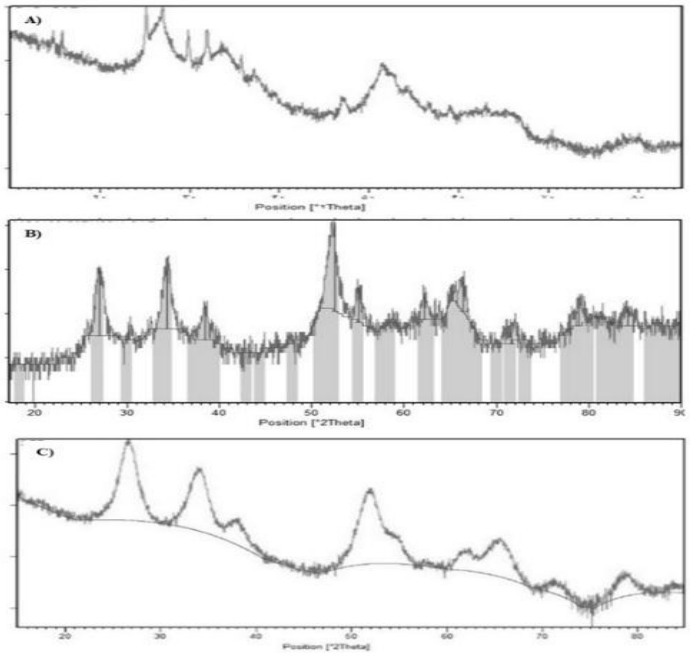

Figure 1: XRD patterns of the synthesized samples: (a) Sample s1, (b) Sample a1, and (c) Sample t1.

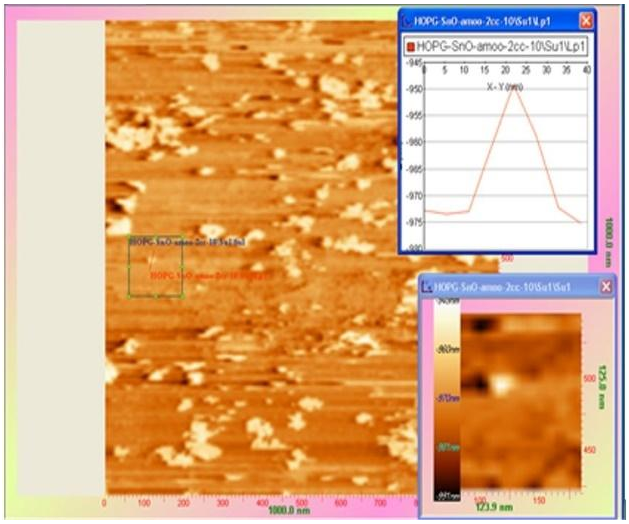

Figure 2: STM image of sample a1 showing nanoparticle morphology.

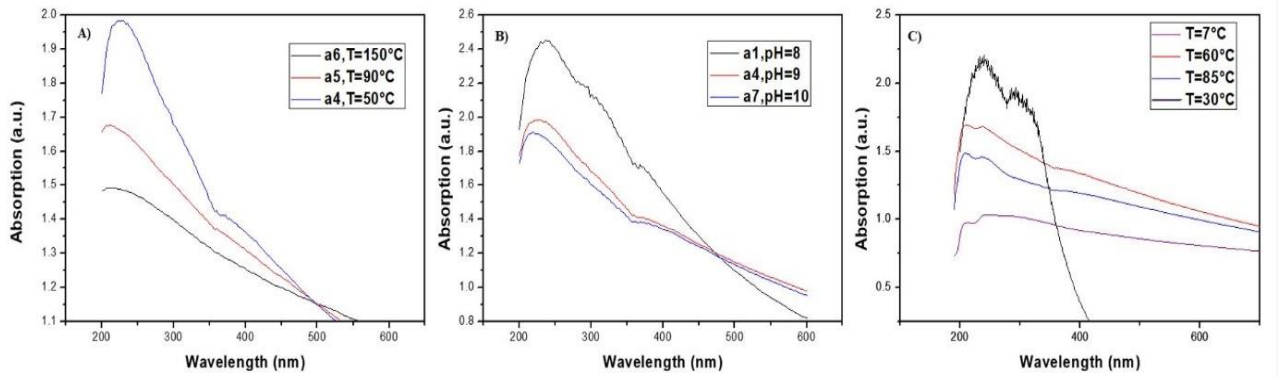

Figure 3. UV-Vis absorption spectra of samples A) a4, a5, and a6 (pH = 9). B) a1, a4, and a7 (T = 50 °C). C) b1, b2, b3, and b4.

Effect of pH at 50 °C:

(Figure. 3B) Increasing pH from 8 to 10 causes a blue shift of the 238 nm peak (larger E_g), while the 296 nm shoulder remains static and the 369 nm feature red-shifts (lower E_g).

Effect of Synthesis Temperature:

(Figure. 3C) The blue-shifts 244 nm peak with temperature, indicating smaller particle sizes. Emergence of absorption shoulders at higher wavelengths aligns with a narrowed size distribution. Table 2 collected detailed of results.

The optical absorption characteristics of SnO_2-based nanoparticles play a crucial role in determining their electronic structure, band gap energy and suitability for optoelectronic and photocatalytic applications. As reported by Mandari et al. (2021), SnO_2 nanoparticles—especially when doped with transition metals such as cobalt—exhibit distinct absorption features in the UV region, with band edge shifts and increased absorption intensity that are indicative of quantum confinement effects and dopant-induced energy states. These features not only affect the optical response but also directly influence charge carrier dynamics, making UV-Vis spectroscopy an essential tool for evaluating modifications in the band structure and optical transitions in synthesized SnO_2 quantum dots [20].

Based on the fitting of the Tauc plots, the following approximate band gap values were estimated:

- **Sample a1 (SnO with minor SnO_2):** ~2.8 eV (direct)
- **Sample t1 (pure SnO_2):** ~3.6 eV (direct)
- **Sample s1 ($Sn_6O_4(OH)_4$ / SnO):** ~2.5 eV

These values confirm that the band gap increases with particle size reduction and phase transformation from SnO to SnO_2 [16].

Urbach energy (E_u) provides insight into the degree of disorder and the presence of localized tail states in the band structure. It was extracted from the slope of the logarithmic absorption coefficient vs. photon energy plot using the Urbach equation [21]:A steeper slope (i.e., lower Eu) indicates a more ordered crystal lattice with fewer defects [22]. The calculated E_u values were: "**Sample t1:** ~0.12 eV, **Sample a1:** ~0.18 eV and **Sample s1:** ~0.25 eV". This trend shows that higher synthesis temperature leads to improved crystallinity and lower structural disorder.

The activation energy reflects the thermal energy required for atomic diffusion and crystallite growth. The calculated values show: "**Sample t1** (T = 373 K): Lower Ea, indicating fast growth kinetics and higher phase purity. **Sample a1** (T ≈ 298 K): Intermediate Ea. **Sample s1** (ambient condition):

Higher Ea, indicating a sluggish growth process with intermediate hydroxide phase formation." Lower activation energies result in faster nucleation and growth rates, consistent with the improved crystallinity observed in XRD and the reduced Urbach energy [23]. Table 3 collected **s**ummary of structural and optical properties samples s1, a1 and t1.

To aim calculate Activation energy, with equation 8 and 9, Activation energy is the slope of diagram logarithm particle size based on (1000/T). So from data from table 4 and slope of diagram from figure 4, the Activation energy is (E_a = 5.03 kJ/mol) [24].

Table 2: Detailed results of UV-Vis absorption spectra of samples with their Eg and size

Sample	Peaks (nm)	Eg (eV)	Size (nm)
a1	238, 296, 379	5.21, 4.19, 3.36	4–7
a4	228, 296, 379	5.44, 4.19, 3.36	4–7
a5	233, 361	5.32, 3.43	4–7
a6	232, 360	5.34, 4.43	4–7
a7	220, 296, 390	5.64, 4.19, 3.26	3–7

Table 3: Summary of Structural and Optical Properties samples s1, a1 and t1.

Sample	Dominant Phase	Crystallite Size (nm)	Band Gap (eV)	Notes
s1	$Sn_6O_4(OH)_4$ + SnO	~34	~2.5	Mixed phase, low temp
a1	SnO (+ minor SnO_2)	~13 (SnO), ~7 (SnO_2)	~2.8	Partially oxidized
t1	SnO_2 (single-phase)	~4	~3.6	Pure phase, thermally annealed

Table 4: Samples b1, b2, b3 and b4 with synthesizes temperature and particle size

Sample Code	Synthesizes temperature (k)	particle size (nm)
b1	280	4
b2	303	4
b3	338	5
b4	358	7

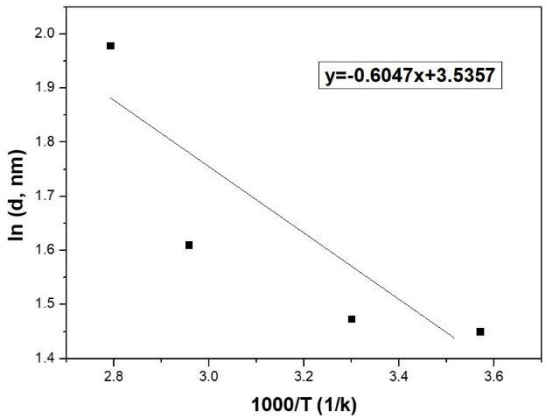

Figure 4: Activation energy plot based on the Arrhenius equation [24]

Using the absorption spectra data of sample a1, a plot of $(\alpha h\nu)^2$ versus photon energy ($h\nu$) was constructed, resulting in Figure 4. Based on this plot, the band gap of the sample is direct.

Figure 5 presents the plots of $(\alpha h\nu)^2$ versus photon energy ($h\nu$) for samples a1, a4, and a7 (nanoparticles synthesized by the co-precipitation method with pH values of 8, 9 and 10 at a heating temperature of 50°C). By extrapolating the data and intersecting with the horizontal axis, the band gap energy values are obtained. The results indicate that an increase in pH leads to an increase in the band gap energy.

To calculate the edge of the energy gap, the Urbach energy for each sample was determined using relation (9). In fact, the Urbach energy is derived from the inverse slope of the ln (α) versus photon energy ($h\nu$) plot, which is presented in Figure 5. The band gap and Urbach energies for the samples are provided in Table 5 [25].

The photoluminescence spectra of samples a1, a4 and a7, excited at a wavelength of 230 nm, are shown in Figure 6, respectively. The emission wavelengths obtained from excitation at 230 nm that appear as multiples of the excitation wavelength are considered unreliable due to their harmonic nature.

Initially, a comparative analysis of the PL spectra for samples a1, a4 and a7 under 230 nm excitation was conducted, followed by a detailed examination of each sample individually. The aim of this comparison was to evaluate the influence of pH on the luminescence behavior of the samples. As observed in Table 6, a minor shoulder around 306 nm appears in the spectra, which transforms into a peak with increasing pH. Peaks, albeit small, also emerge at 362 nm and 383 nm with rising pH. A prominent peak at 407 nm is observed, whose intensity diminishes as the pH increases. A shoulder at 428 nm is initially presented but disappears at higher pH levels. The most intense peak is observed at 460 nm, which increases in intensity with rising pH and is indicative of the second harmonic emission. Additionally, a shoulder at 484 nm is noted to shift towards longer wavelengths as the pH increases. A minor shoulder is also observed around 532 nm. With further increase in pH, a distinct peak develops at 575 nm, while another emission peak appears at 686 nm, which is again attributed to second-order harmonic emission.

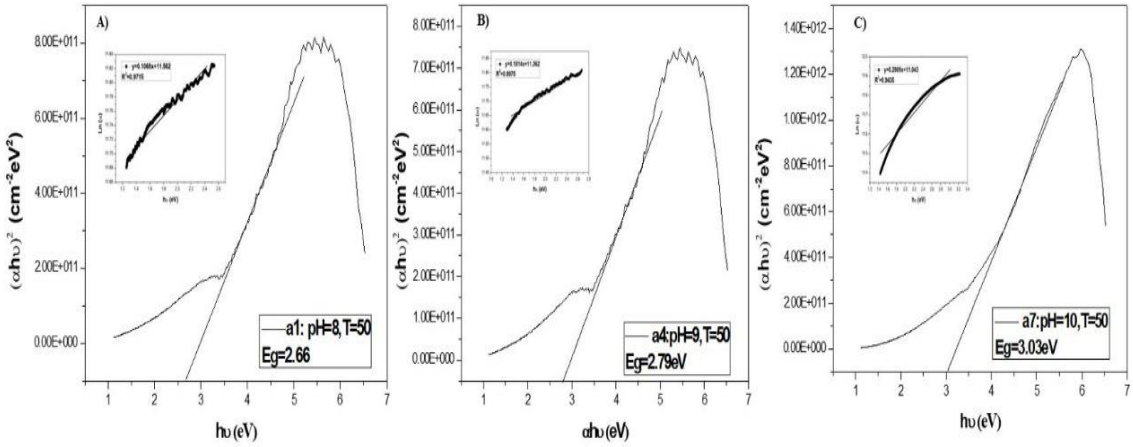

Figure 5: Energy gap of sample A) a1, B) a4 and C) a7

Table 5: The band gap and Urbach energies for the samples (a1, a4, a7)

Sample	E_g (eV)	E_u (eV)
a1	2.66	0.369
a4	2.79	0.515
a7	3.03	0.343

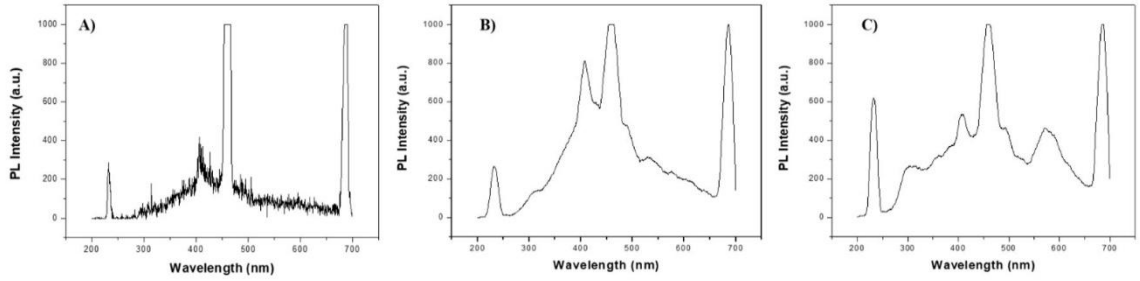

Figure 6: photoluminescence with excitation (230 nm) sample: A) a1, B) a4 and C) a7

Samples a1, a4, and a7 were visually examined in a dark room under UV lamps which Visual observation with wavelengths of 360 nm and 370 nm.[26]. Samples a1 and a7 exhibited minimal color change under 360 nm illumination, whereas sample a4 appeared distinctly purple. When exposed to 370 nm light, samples a1 and a7 displayed a blue coloration, while sample a4 again exhibited a purple hue, confirming PL spectral shifts with pH [27, 28]. In the context of photoluminescence properties of SnO_2 nanoparticles, previous studies have shown that the aspect ratio and structural parameters significantly influence their optical behavior. Kolokolov et al. examined the synthesis of SnO_2 nanoparticles with different aspect ratios and their corresponding photoluminescent properties [29]. Their study revealed that the photoluminescence intensity and emission characteristics are closely related to the particle shape and size, as well as the synthesis conditions, such as pH and temperature. These structural variations directly impact the electronic properties of the material, which in turn influence its photocatalytic efficiency. The observed shifts in the PL spectra were attributed to the quantum confinement effects and the presence of surface states, which are common in nanomaterials. Additionally, the article discusses the rapid degradation of organic dyes as a function of the nanoparticle's PL properties, demonstrating the strong potential of SnO_2 nanoparticles for photocatalytic applications [29].

Further insights into the improvement of photoluminescence and photocatalytic efficiency of SnO_2 quantum dots have been provided by the study of niobium-modified SnO_2 QDs (Yousefzadeh et al., 2021). In this work, Nb incorporation led to enhanced visible-light absorption and stronger PL emission, attributed to the introduction of localized energy states within the band gap. These defect-related states facilitate more efficient charge separation and reduced recombination rates, thereby improving the photocatalytic performance under visible light. The findings suggest that controlled doping of SnO_2 QDs is an effective strategy to tailor their optical and electronic properties, making them more suitable for applications in environmental remediation and optoelectronic devices [30].

Table 6. Summary of Photoluminescence Peaks for Samples a1, a4, and a7 under 230 nm Excitation

Wavelength (nm)	Observation Type	Behavior with Increasing pH	Notes
~306	Shoulder	Converts to distinct peak	Suggests increased emission efficiency
362	Minor peak	Slight increase in intensity	Possibly defect-related states
383	Minor peak	Slight increase in intensity	
407	Major peak	Decreases in intensity	Dominant emission; quenched with higher pH
428	Shoulder	Disappears with pH increase	Possibly unstable emission state
460	Strongest peak	Intensifies with increasing pH	Corresponds to second harmonic
484	Shoulder	Redshifts with increasing pH	Indicative of band structure modification
532	Weak shoulder	Remains relatively unchanged	
575	Emergent peak	Grows in intensity with pH	Related to deeper defect states
686	Broad peak	Present; possibly harmonic-related	Attributed to second-order harmonic

CONCLUSION

In this work, the co-precipitation method was successfully employed to synthesize quantum-sized Tin Oxide nanoparticles, including SnO, SnO_2 and the intermediate $Sn_6O_4(OH)_4$ phase. Comprehensive XRD analysis revealed phase evolution driven by synthesis temperature and pH, while STM confirmed a particle size range of approximately 4–20 nm. Optical characterization via UV–Vis spectroscopy showed significant quantum confinement effects, with the direct band gap ranging from ~2.5 eV for mixed phases to ~3.6 eV for pure SnO_2. Band gap values were further corroborated by Tauc plot fitting, confirming direct electronic transitions. The electro-structural disorder, quantified by Urbach energy (Eu), decreased from 0.25 eV (s1) to 0.12 eV (t1), indicating improved crystallinity with higher annealing temperatures. The activation energy for particle growth was estimated at ~5 kJ/mol, reflecting facile synthesis kinetics. Photoluminescence studies demonstrated pH-dependent emission shifts, suggesting tunable optoelectronic properties [5, 22].

Our findings align well with previous reports on SnO_2 quantum dots. For instance, Saravanan et al. synthesized ~2.5 nm SnO_2 QDs with a band gap of ~3.67 eV and strong quantum confinement via a solvothermal route [31]. Similarly, recent reviews on SnO_2 QDs note band gaps in the 3.5–4.0 eV range and highlight their tunable optical and photocatalytic properties. Urbach energy analysis of various SnO_2 nanoparticles revealed values comparable to our data, confirming the correlation between structural order and optical absorption tailing. Furthermore, the importance of band gap tuning via oxygen vacancies or doping for enhanced visible-light response has been emphasized in recent works [28].

Compared to bulk SnO_2 (Eg ~3.6 eV), our nanoparticle systems provide broader tunability in optical and electronic properties. The observed increase in band gap with decreasing particle size is consistent with Brus's quantum confinement model [5, 28].

As a hole:

- Co-precipitation reliably produced quantum-sized SnO and SnO_2 phases.
- XRD confirms phase evolution controlled by pH and thermal conditions.
- STM and UV–Vis show size control in the 4–20 nm range, inducing significant quantum confinement (blue-shifted E_9 from ~2.6 to >5.6 eV).
- pH increase raises E_9 and alters E_u, indicating optimized structural/facial quality at higher pH.
- Activation energy (5.03 kJ/mol) is relatively low, suggesting facile nucleation/drying-driven growth.
- PL shifts with pH suggest tunable optical properties, valuable for optoelectronic or sensing applications [11].

REFERENCES

1. Mendes PG, Moreira ML, Tebcherani SM, Orlandi MO, Andrés J, Li MS, et al. SnO2 nanocrystals synthesized by microwave-assisted hydrothermal method: towards a relationship between structural and optical properties. Journal of Nanoparticle Research. 2012;14(3).

2. Kumari K, Ahmaruzzaman M. SnO2 quantum dots (QDs): Synthesis and potential applications in energy storage and environmental remediation. Materials Research Bulletin. 2023;168.

3. Chen D, Huang S, Huang R, Zhang Q, Le T-T, Cheng E, et al. Highlights on advances in SnO2 quantum dots: insights into synthesis strategies, modifications and applications. Materials Research Letters. 2018;6(9):462-88.

4. Mussabekova AK, Zeinidenov AK, Tazhibayev SK, Omarbekova GI, Abeuov DR, Aimukhanov AK. The influence of surface defects in SnO2 thin films prepared from different alcohol solvents on electron transport in polymer solar cells. Synthetic Metals. 2025;313.

5. Bathula B, Gurugubelli TR, Yoo J, Yoo K. Recent Progress in the Use of SnO2 Quantum Dots: From Synthesis to Photocatalytic Applications. Catalysts. 2023;13(4).

6. Vandana M, Veeresh S, Ganesh H, Nagaraju YS, Vijeth H, Basappa M, et al. Graphene oxide decorated SnO2 quantum dots/polypyrrole ternary composites towards symmetric supercapacitor application. Journal of Energy Storage. 2022;46.

7. Manouchehri SB, Parviz; Marasi, Atefe; Amoo, Maryam; , Yousefi MH. Synthesis of Single Phase Tin(II) Oxide Nanoparticles by Microwave-Assisted Hydrothermal Technique. Iran J Chem Chem Eng 2018;37(6):1-8.

8. Komal K, Singh M, Singh B. Effect of rGO weight percentage on structural, optical, and electrical properties of rGO-SnO2 nanocomposite for resistive memory device applications. Materials Science and Engineering: B. 2024;303.

9. Jouhannaud J, Rossignol J, Stuerga D. Rapid synthesis of tin (IV) oxide nanoparticles by microwave induced thermohydrolysis. Journal of Solid State Chemistry. 2008;181(6):1439-44.

10. Majumdar S, Chakraborty S, Devi PS, Sen A. Room temperature synthesis of nanocrystalline SnO through sonochemical route. Materials Letters. 2008;62(8-9):1249-51.

11. Mohana Priya S, Geetha A, Ramamurthi K. Structural, morphological and optical properties of tin oxide nanoparticles synthesized by sol–gel method adding hydrochloric acid. Journal of Sol-Gel Science and Technology. 2016;78(2):365-72.

12. Krishnakumar T, Jayaprakash R, Parthibavarman M, Phani AR, Singh VN, Mehta BR. Microwave-assisted synthesis and investigation of SnO2 nanoparticles. Materials Letters. 2009;63(11):896-8.

13. VD Mote YPaBD. Williamson-Hall analysis in estimation of lattice strain in nanometer-sized ZnO particles. Journal of Theoretical and Applied Physics. 2012;6(6):1-8.

14. Yang L, Yang Y, Liu T, Ma X, Lee SW, Wang Y. Oxygen vacancies confined in SnO2nanoparticles for glorious photocatalytic activities from the UV, visible to near-infrared region. New Journal of Chemistry. 2018;42(18):15253-62.

15. Javaid S, Farrukh MA, Muneer I, Shahid M, Khaleeq-ur-Rahman M, Umar AA. Influence of optical band gap and particle size on the catalytic properties of Sm/SnO2–TiO2 nanoparticles. Superlattices and Microstructures. 2015;82:234-47.

16. Selvamani K, Sasikala S, Kalaiselvi V. Synthesis and Characterization of Tin oxide and Zinc Doped Tin Oxide Nanoparticles by Chemical Precipitation Method. International Journal of Advanced Science and Engineering. 2020;7(1):1629-32.

17. Al-Gaashani R, Radiman S, Tabet N, Daud AR. Optical properties of SnO2 nanostructures prepared via one-step thermal decomposition of tin (II) chloride dihydrate. Materials Science and Engineering: B. 2012;177(6):462-70.

18. Sayeed MA, Rouf HK. Al-doped SnO2 thin films: impacts of high temperature annealing on the structural, optical and electrical properties. Journal of Materials Research and Technology. 2021;15:3409-25.

19. Thenmozhi. C MV, Kumar.E, Veera Rethina Murugan. S. Synthesis and Characterization of SnO2 and PANI Doped SnO2 Nanoparticles by Microwave Assisted Solution Method. International Research Journal of Engineering and Technology 2015;2(9):2634-40.

20. Entradas T, Cabrita JF, Dalui S, Nunes MR, Monteiro OC, Silvestre AJ. Synthesis of sub-5 nm Co-doped SnO2 nanoparticles and their structural, microstructural, optical and photocatalytic properties. Materials Chemistry and Physics. 2014;147(3):563-71.

21. Chetri P, Choudhury A. Investigation of optical properties of SnO2 nanoparticles. Physica E: Low-dimensional Systems and Nanostructures. 2013;47:257-63.

22. Pramothkumar A, Vivek E, Sabari Girisun TC, Meena M, Vetha Potheher I. A comparative analysis on electrical and nonlinear optical properties of pure and Co–Ni co-doped SnO2 nanoparticles. Optical Materials. 2022;130.

23. Dhinakar KG, Sundar SM. Structural & Optical Properties of Co DOPED SnO2 Nanoparticles Synthesised By Microwave Assisted Solvothermal Method. IOSR Journal of Applied Physics. 2017;03(01):92-7.

24. Uysal BÖ, Arıer ÜÖA. Structural and optical properties of SnO2 nano films by spin-coating method. Applied Surface Science. 2015;350:74-8.

25. Hou S, Wu S, Luo J, Ali HE, Eli S. SnO2 nano particles Co-doped by Co and Ag: Microstructural, photocatalytic, magnetic, and Electric studies. Vacuum. 2023;212.

26. Sobhanan J, Rival JV, Anas A, Sidharth Shibu E, Takano Y, Biju V. Luminescent quantum dots: Synthesis, optical properties, bioimaging and toxicity. Adv Drug Deliv Rev. 2023;197:114830.

27. Singhal A, Sanyal B, Tyagi AK. Tin oxide nanocrystals: controllable synthesis, characterization, optical properties and mechanistic insights into the formation process. RSC Advances. 2011;1(5).

28. Babu B, Neelakanta Reddy I, Yoo K, Kim D, Shim J. Bandgap tuning and XPS study of SnO2 quantum dots. Materials Letters. 2018;221:211-5.

29. Kolokolov DS, Podurets AA, Nikonova VD, Vorontsov-Velyaminov PN, Bobrysheva NP, Osmolowsky MG, et al. SnO2 nanoparticles with different aspect ratio and structural parameters: fabrication, photocatalytic efficiency dependences and fast organic dyes degradation. Applied Surface Science. 2022;599.

30. Wang Y, Su N, Liu J, Lin Y, Wang J, Guo X,

et al. Enhanced visible-light photocatalytic properties of SnO2 quantum dots by niobium modification. Results in Physics. 2022;37.

31. Karimi-Maleh H, Karimi F, Malekmohammadi S, Zakariae N, Esmaeili R, Rostamnia S, et al. An amplified voltammetric sensor based on platinum nanoparticle/polyoxometalate/two-dimensional hexagonal boron nitride nanosheets composite and ionic liquid for determination of N-hydroxysuccinimide in water samples. Journal of Molecular Liquids. 2020;310:113185.